Marquette University
e-Publications@Marquette

4-1-2013

Using Micro-Raman Spectroscopy to Assess MEMS Si/SiO2 Membranes Exhibiting Negative Spring Constant Behavior

Lavern A. Starman
Air Force Institute of Technology

Ronald A. Coutu Jr.
Marquette University, ronald.coutu@marquette.edu

Electrical and Computer Engineering Faculty Research and Publications/College of Engineering

Contents

Using Micro-Raman Spectroscopy to Assess MEMS Si/SiO$_2$ Membranes Exhibiting Negative Spring Constant Behavior

L. A. Starman
Air Force Institute of Technology, Wright-Patterson Air Force Base, OH
R. A. Coutu Jr.
Air Force Institute of Technology, Wright-Patterson Air Force Base, OH

Abstract

We introduce a novel micro-mechanical structure that exhibits two regions of stable linear positive and negative stiffness. Springs, cantilevers, beams and any other geometry that display an increasing return force that is proportional to the displacement can be considered to have a "Hookean" positive spring constant, or stiffness. Less well known is the opposite characteristic of a reducing return force for a given deflection, or negative stiffness. Unfortunately many simple negative stiffness structures exhibit unstable buckling and require additional moving components during deflection to avoid deforming out of its useful shape. In Micro-Electro-Mechanical Systems (MEMS) devices, buckling caused by stress at the interface of silicon and thermally grown SiO$_2$ causes tensile and compressive forces that will warp structures if the silicon layer is thin enough. The 1 mm^2 membrane structures presented here utilizes this effect but overcome this limitation and empirically demonstrates linearity in both regions. The Si/SiO$_2$ membranes presented deflect ~17 μm from their pre-released position. The load deflection curves produced exhibit positive linear stiffness with an inflection point holding nearly constant with a slight negative stiffness. Depositing a 0.05 μm titanium and 0.3 μm layer of gold on top of the Si/SiO$_2$ membrane reduces the initial deflection to ~13.5 μm. However, the load deflection curve produced illustrates both a linear positive and negative spring constant with a fairly sharp inflection point. These results are potentially useful to selectively tune the spring constant of mechanical structures used in MEMS. The structures presented are manufactured using typical micromachining techniques and can be fabricated *in-situ* with other MEMS devices.

Introduction

Numerous micro-mechanical devices such as cantilevers, beams, and springs display an increasing return force that is proportional to its displacement. Such devices can be considered to have a "Hookean" positive spring constant, or stiffness. While the opposite effect, a reducing return force for a given deflection is less well known, this effect has been in use for many decades.[1] Stress at the interface of silicon and thermally grown silicon dioxide (SiO_2) is inherently unavoidable, and can cause buckling in Micro-Electro-Mechanical Systems (MEMS) devices. As the oxide forms on the surface of the silicon, the tendency for it to expand to its natural density is constrained by the interfacial bond and the oxide surrounding it. This causes tensile and compressive forces to develop which will warp structures if the silicon layer is relatively thin. The membrane structure presented here requires this deformation for proper operation. Simple cantilevers, beams and membrane structures operate through the use of potential energy being added to their systems as a result of structural displacement occurring.[2,3] At some point in their deflection, the potential energy begins to aid in the deformation of the structure, reducing the force required for further displacement. Unstable systems can require moving constraints during deflection so as not to deform out of useful shape. Complex devices that mimic a negative linear stiffness are often used in large vibration isolation systems;[4] however, they are not practical on the MEMS scale. Recent MEMS research has attempted to use other methods to provide for negative stiffness, such as electrostatic forces.[5]

In this paper, we introduce and characterize a novel micro-mechanical membrane structure that incorporates deformation due to the interfacial stresses between silicon and thermally grown SiO_2 that empirically demonstrates similar spring return force characteristics of the disk cone spring shown in Fig. 1(a). Several 16 element, 1 mm^2 membranes were fabricated with a membrane composition consisting of a 5 μm silicon layer and a 2 μm SiO_2 layer. Figure 1(b)shows the preliminary results for a typical Si/SiO_2 membrane fabricated using standard micromachining techniques which exhibits similar characteristics to the disk cone spring.[6] When adding a 0.35 μm thin layer of titanium and gold to the membrane, the structure self constrains such that it exhibits stable linear positive and negative stiffness. These membrane structures are the first known devices to incorporate linearity in both regions. In addition, by limiting the deflection of the structure to only the negative stiffness region essentially creates the first linear negative stiffness micro-mechanical spring. Negative stiffness is potentially useful for selectively tuning the spring constant of micro-mechanical beams found in MEMS sensors and actuators.
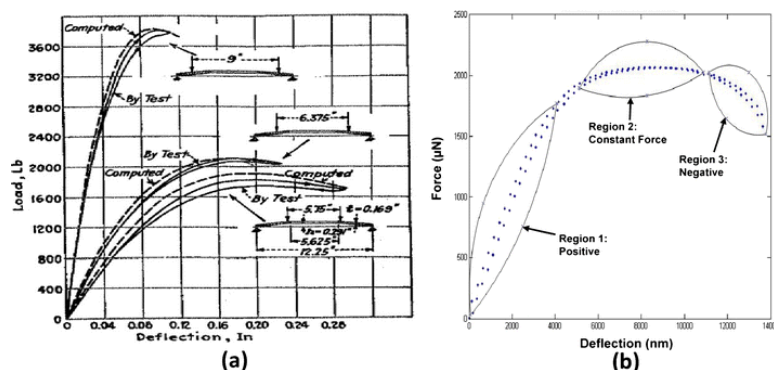

Fig. 1 (a) illustrates the load deflection plots for a macro scale center disk spring[1] Reprinted with permission from J.O. Almen and A. Laszlo, Transactions of ASME Publications, Volume Number RP-58-10, 1936, and (b) shows the measured output load deflection for a micro-scale Si/SiO_2 membrane from this research effort[6]

Background

A MEMS structure which exhibits similar load deflection characteristics as our Si/SiO$_2$membrane presented is the centrally clamped bistable silicon mechanism shown in Fig. 2(a)with its accompanying force vs. deflection plot shown in Fig. 2(b).[7] The centrally-clamped device has a length of 3 mm, a width of 10 μm and a thickness of 480 μm.[7] The device dimensions presented for our research are 1 mm^2 membranes having a thickness of ~7 μm. Although the structures are significantly different, the similarities in their operation can provide valuable insight into the overall operation of the fabricated Si/SiO$_2$ membranes.
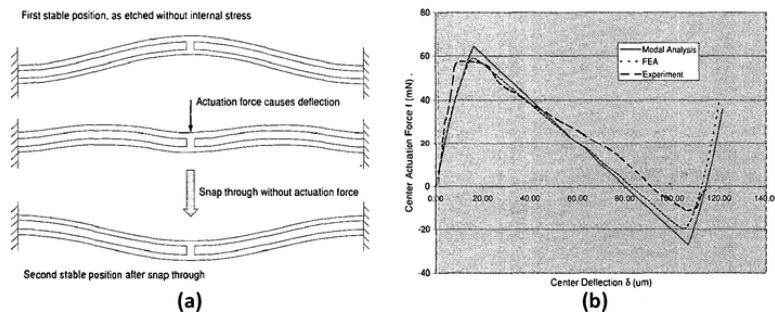

Fig. 2 (**a**) Fixed supported beam with center connection provides the load curves in (**b**) showing the linear region of deflection curve[7] © 2001 IEEE, Reprinted, with permission, from IEEE Proceedings from the 14th IEEE International Conference on Micro Electro Mechanical Systems, MEMS 2001

Thin Film Stress

Stress develops in thin films due to a variety of reasons, including mismatched lattice constants, different coefficients of thermal expansion between materials, and as a result of the growth process [8]. Residual stress in thin films can influence dopant diffusion, affect hot carrier degradation and jeopardize oxide reliability. In MEMS, residual stress and residual stress gradients through the thickness of a film are critical constraints on microstructure designs. If the average residual stress is compressive for example, micro-bridges buckle if longer than a critical length while stress gradients generate an internal bending moment that causes micro devices to warp (up or down) out-of-plane upon release.[9] Residual stress has a significant dependence on film thickness in which the highest compressive stress during deposition is created in the first 200 nm and begins to relax significantly if the film becomes thicker than 350 nm.[10]

Negative Stiffness/Spring Constant

Based on the parameters which make up the equation for the spring constant (equation (3)), for a given material (fixed Young's Modulus), one can mechanically modify the spring constant by making physical changes in the geometry of the structure.[11,12,13] Some of these modifications could be impractical due to size constraints or they may exhibit undesirable displacement sensitivity effects. An alternative method to decrease the overall effective spring constant is to offset it with a negative stiffness.

Negative structural stiffness is fundamentally a reduction in return force for a given displacement. The mechanical realization of this concept has been used and studied for over 80 years.[1,14] Many objects which demonstrate this are pre-strained, in a post-buckled state, require potential energy through pre-loading[15] and can only produce it non-linearly. Dynamic modeling of these devices is generally constrained to small relative displacements so that linearization can be assumed allowing for easier

design. Figure 3(a) illustrates a simple spring system which demonstrates a typical theoretical load deflection plot shown in Fig. 3(b)for a negative stiffness system.
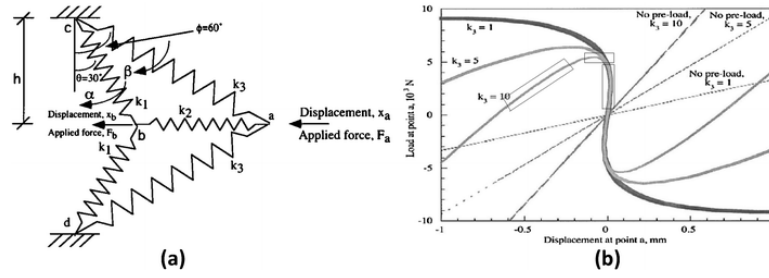

(a)   (b)

Fig. 3 (a) Equivalent resistive model of membrane, **(b)** load displacement curves of resistive model if point 'a' is restricted to only move in a horizontal plane.[15] Reprinted with permission from Y.C. Wang and R.S. Lakes, American Journal of Physics, Vol. 72, Page 40, 2004

Stiffness, also known as a spring constant, is the slope at any point in the plot. Initially, the $k_1$and k_3 springs shown in Fig. 3(a) are in a non-loaded state with the upper and lower ends attached to fixed pivots (point's c and d). The center spring k_2, is only free to move horizontally. As point 'a' in Fig. 3(a) is deflected to the left, the k_1, k_2 and k_3 springs are compressed, forcing point 'b' to also move to the left, such that potential energy is added to the system and the force increases to the right. This is demonstrated as the linear positive stiffness of $k_3 = 10$ shown in Fig. 3(b). When the spring forces are in equilibrium around the midpoint, no force is produced right or left, and the system is at the unstable zero point as shown in Fig. 3(b). Any additional deflection past this point results in the springs developing a force to the right and popping through as indicated by the spring values above the '0' displacement position in Fig. 3(b). Negative stiffness is demonstrated after the inflection point up to the zero point. All key regions of the spring force are illustrated by rectangular boxes in Fig. 3(b) along the $k_3 = 10$ line.

Other research has concentrated on using active systems to produce a negative spring constant, such as with electrostatic forces. These systems of course require external power, and the development of effective control systems is ongoing.[16] This research presents the results from the modification of a passive system, the buckled oxide membrane.

Design

The electrical operation of many MEMS devices can depend on spatial changes between surfaces or even the bending of materials which in turn change their electrical properties. Small changes in distances can easily be detected through capacitive sensing circuits and the flexing of piezoresistive materials can be measured through changes in electrical potential. For example, the displacement of a fixed-fixed beam, where the applied force is a point load at the center of the beam's length is given by[17]

$$y = \frac{FL^3}{192EI} \text{ (1)}$$

where, F is the applied force, L is the length of the beam, E is the Young's Modulus of the beam material and I is the moment of inertia. If we only consider rectangular structures, the moment of inertia is given by

$$I = \frac{wt^3}{12} \text{ (2)}$$

in which w is the width of the beam and t is the thickness of the beam with the bending moment about the x-axis. The spring constant is determined from Hooke's Law $k = F/y$ where, F is the applied force and y is the displacement.[17] The spring constant for a fixed-fixed beam can be determined by applying Hooke's law to equation (1) and then solving for the spring constant k.

$$k = \frac{16Ewt^3}{L^3} \text{ (3)}$$

When we evaluate MEMS inertial sensors, these devices typically use a suspended mass which is attached by tethers to the surrounding bulk material to enable small, measurable displacements.[18] This displacement can be viewed similarly to the fixed-fixed beam described above in which the suspended mass acts as the point load force with the tethers being modeled as the beam. Therefore, the tether's thickness, length, shape and the material used all determine the required spring constant for displacement sensitivity and the resonant frequency as shown in equations (4) and (5)

$$S_d = \frac{ma}{k} \text{ (4)}$$

$$f_{res} = \frac{\pi}{2}\sqrt{\frac{k}{m}} \text{ (5)}$$

where, a is the acceleration, m is the mass and k is the spring constant. As shown in the above equations, both the mass and the spring constant inversely affect the sensitivity and resonant frequency. For example, if the mass is increased, the sensitivity increases; however, the resonant frequency decreases. The opposite effect is true if the spring constant is changed. Therefore, since a change in mass has opposing effects on the sensitivity and resonance, the mass will be considered a constant in this research. This assumption allows us to focus on the spring constant variable which is the focal point of this paper.

Analytical Modeling

To quantify the deflection of the Si/SiO$_2$ membrane following the deep reactive ion etch, two different models will be used. Since our fabricated structure is a square membrane, the first model consists of a load deflection of square membranes. The second model will access the stress within the membrane as a uniform load on a fixed-fixed microbridge. This stress model will aid in the characterization of the stress profiles obtained from micro-Raman spectroscopy.

Load deflection of square membranes

Although the solutions for small deflection theory and membrane theory are well known,[19,20,21,22] the theory is briefly repeated here for completeness. For small deflections, thin film plate theory deflection is said to be dominated by the resistance of the membrane to bending. Tabata et al.[19] developed an analytical solution for the load-deflection relationship for rectangular membranes. This relationship between the external load and the membrane deflection makes it possible to determine the residual stress and Young's modulus of thin films. The load-deflection behavior is of the form

$$p = \frac{C_1 \sigma t h}{d^2} + \frac{C_2 E t h^3}{d^4} \quad (6)$$

where, p is the applied pressure, h is the center deflection, d is one half of the membrane's edge length, t is the membranes thickness, E is the Young's modulus, σ is the residual stress, and ν is the in-plane Poisson's ratio. The values C_1 and C_2 are numerical constants which are determined by the membranes shape $b/a = 1/n$ where a and b are the length and width of the membrane which is used only to define the variable "n", thus for a square membrane such as our device presented, $(n = 1)$. The constants C_1 and C_2 are derived from the following equations[19]

$$C_1 = \frac{\pi^4(1+n^2)}{64} \quad (7)$$

And

$$C_2 = \frac{\pi^6}{32(1-\nu^2)} \left\{ \frac{9+2n^2+9n^4}{256} - \left[\frac{(4+n+n^2+4n^3-3n\nu(1+n))^2}{2\{81\pi^2(1+n^2)+128n+\nu[128n-9\pi^2(1+n^2)]\}} \right] \right\} \quad (8)$$

Maier-Schneider et al.[20] slightly modified the above equations to account for the real bending behavior of a silicon nitride membrane by taking into account the effects of Poisson's ratio and Young's modulus to obtain values for C_1 and C_2 to be 3.45 and 2.48 respectively. These values for C_1 and C_2 closely match finite element analysis (FEM) results determined by Pan et al.[21] for silicon nitride.

For the Si/SiO$_2$ membrane fabricated in this research effort, the constants C_1 and C_2 are analytically determined to be 3.04 and 1.83 respectively. These values for C_1 and C_2 are slightly different from the previous work by Maier-Schneider et al.[20] due to the different Poisson's ratio and Young's modulus for the Si/SiO$_2$ membrane verse the SiN membrane. Through interpolation from the membrane material properties, the residual stress is calculated to be 72.14 MPa and Young's modulus is 110.71 GPa. By applying these values, the analytically derived applied pressure as determined from equation (6) is 0.149 MPa.

For the second membrane (i.e. titanium and gold layers added), the equivalent interpolated Poisson's ratio slightly increased to 0.255, Young's modulus decreased slightly too approximately 109.42 GPa and the residual stress increased to approximately 80.95 MPa. The constants C_1 and C_2 remain approximately the same while the applied pressure increased slightly too approximately 0.166 MPa. This slight increase is a result of the additional tensile stress in the thin metal layers deposited onto the membrane.

Uniform load fixed-fixed beam stress profile

An analytical microbridge beam stress profile was created to provide insight into the stress profile characteristics obtained using micro-Raman spectroscopy. This model was selected since a narrow fixed-fixed beam could realistically replicate the stress profile for a square membrane. A narrow beam slice through the center and across the membrane will experience slight torsion and twisting effects; however, these effects will be minimal and not be considered in this model. This analytical solution provides insight into the residual stress profile for a freestanding microbridge beam. The analytical model uses a uniform distributed load g as shown in Fig. 4(a). R_1 and R_2 are the resultant forces, and M_1 and M_2 are the moments about the microbridge beam.[23]
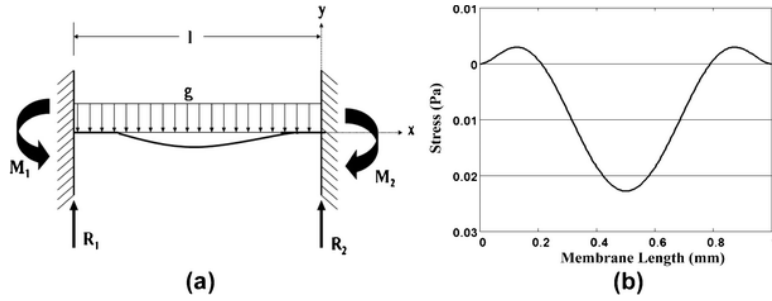
Fig. 4 (a) Analytical stress model for a MEMS microbridge beam assuming a uniform distributed load and **(b)** stress profile obtained for a small, distributed load[17]

For a released microbridge beam with a uniform distributed load, the residual stress can be calculated by the following equation[23]

$$\sigma = \frac{M(x)y}{I} \, (Pa) \text{ (9)}$$

where $M(x)$ is the moment about the beam and is given by[23]

$$M(x) = \frac{g}{12}(6lx - 6x^2 - l^2)(N/m) \text{ (10)}$$

where g is the distributed load, l is the beam length, and x is a selected position along the length of the beam respectively. For the analytical stress model calculation plotted in Fig. 4(b), the value of x was stepped from 0 to 1000 μm (model beam length). The compressive residual stress along the length of the beam can be assessed to be a uniform load since this stress will produce a constant, uniform applied force within the material layer. Although the stress magnitudes for this simplified model for the microbridge are small due to the minimal uniform load applied, the experimentally measured Raman stress profiles presented later for a released membrane clearly resembles the stress profile shown in Fig. 4(b) for a microbridge beam.

The SOI wafer used in this research has a 2 µm thick oxide layer with a 5 µm thick silicon device layer. Once the deep reactive ion etch (DRIE) is complete, the 7 µm thick membrane consisting of the oxide and the silicon device layer will deflect due to the inherent residual stresses. Thermally grown SiO₂ residual stress values are approximately 300 MPa compressive while the residual stress in the crystalline silicon device layer should be small due to minimal vacancies, interstitials, and stress gradients.

Finite Element Modeling

To assess the deflection of the Si/SiO₂ membrane following the DRIE, an FEM model was developed using CoventorWare[24] to observe peak stress locations and membrane deflection magnitudes. The model consisted of a stacked 1 mm² Si/SiO₂ membrane in which all edges of the membrane are fixed in the x- and y-directions such that deflection only occurs in the z-direction. A Manhattan brick mesh of $10 \times 10 \times 2\mu m$ was used for all Si/SiO₂ membrane simulations. From experimental membrane deflection results, the models internal stresses were set to obtain the approximate 17 µm deflection of the released membrane. From De Wolf,[25] nearly all inherent residual stress in a Si/SiO₂ stacked material lies within the oxide layer. The silicon device layer has minimal stress due to its crystalline structure as stated by Best.[26] The above statements by De Wolf and Best held true for this Si/SiO₂ membrane

simulation in that the model required approximately 240 MPa of compressive stress be integrated into the oxide material layer and 5 MPa to the silicon layer to reach our 17 μm measured deflection.

A second FEM model was developed to assess the effects the 500 Å titanium and 3000 Å gold layers have on the overall deflection and functionality of the Si/SiO_2 membrane. The material stress parameters for the silicon and oxide layers remained the same from the Si/SiO_2membrane simulation. Due to the thin titanium layer's inability to be meshed with Manhattan Brick elements, a parabolic mesh was selected for all layers using an element size of 50 μm to minimize simulation times. The residual stress values for the titanium and gold layers were set to be 65 MPa and 25 MPa respectively. Figure 5(a) shows an example 3D membrane deflection image obtained from CoventorWare for the Si/SiO_2 membrane and Fig. 5(b) provides a 2D profile comparing the peak deflections from the Si/SiO_2 membrane and the Si/SiO_2 membrane incorporating the Ti/Au metal layers. As shown in Fig. 5(b) the displacement magnitude of the Si/SiO_2 membrane decreased from approximately 17 μm to 13.5 μm with the additional metal layers. This reduced deflection is a result of the added material thickness encompassing the membrane (i.e. 7 μm to 7.35 μm), and the tensile stress of the metal layers. From theory, both the membrane thickness and the additional tensile stress should diminish the peak membrane deflection as the model illustrates.
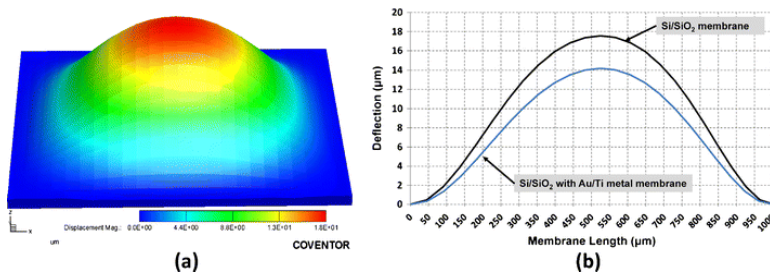

Fig. 5 FEM membrane deflection image for (**a**) 3D Si/SiO_2 stacked membrane illustrating the peak deflection magnitude and (**b**) shows a comparison of the deflection profiles for the Si/SiO_2 stacked membrane and the Si/SiO_2 stacked membrane with Ti/Au metals. The added metal layer reduced the peak membrane deflection by ~4 μm

Membrane Fabrication

The Si/SiO_2 membrane was fabricated using a Silicon-On-Insulator (SOI) wafer from Ultrasil Corporation. The membrane consists of a 2 μm thick SiO_2 layer thermally grown on the silicon substrate. A second wafer (device layer) is then bonded to the oxide and thinned via chemical mechanical polishing (CMP) to a thickness of 5 μm. Both the device and substrate layers were n-type, <100> monocrystalline silicon with layer thicknesses of 5 and 400 μm respectively. In addition to being a component material layer in the membrane, the 2 μm buried oxide layer also served as a natural etch stop for the DRIE process. For this research effort, two different device membranes are fabricated; 1) a Si/SiO_2 membrane and, 2) a Si/SiO_2 membrane with the additional metal layer consisting of 500 Å titanium/3000 Å gold. This metal layer was deposited on top of the device layer prior to the DRIE. Figure 6 shows an optical image of two elements of a 16 element Si/SiO_2 membrane with the additional Ti/Au metal layer. Figure 6(a) shows a top view of two elements while Fig. 6(b) shows the same two elements as viewed from the backside of the wafer. Figure 6(c) shows an interferometric microscope (IFM) image, with membrane dimensions labeled, of the top of the membrane illustrating the inward deflection of the membrane as observed by the fringe lines identifying the edges of the membrane.
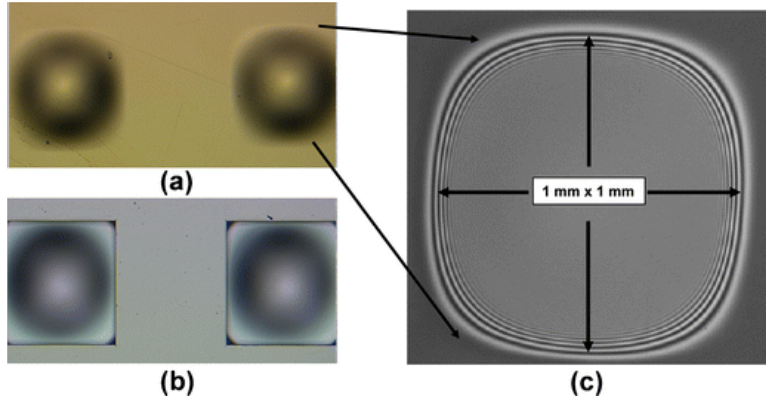
Fig. 6 Optical images of the fabricated Si/SiO$_2$ membrane with the Ti/Au metal layer. (**a**) a two element membrane image as observed from the top surface, (**b**) the same two element membrane as observed from the backside of the wafer showing the bottom side of the membrane, and (**c**) an IFM image illustrating the deflection of the membrane as observed by the optical fringe lines while showing the physical dimensions of the membrane

The backside wafer preparation began with the deposition of a 3 µm plasma enhanced chemical vapor deposition (PECVD) SiO$_2$ layer. A 2 µm thick photoresist layer was used to pattern the PECVD oxide layer to define the backside of the square membranes. The patterned photoresist was developed to expose the oxide layer which was then etched using a buffered oxide etch (BOE). The patterned oxide now becomes a robust mask layer which is necessary for the lengthy silicon substrate DRIE etch. Lastly, the silicon substrate is etched through the backside window all the way to the buried topside oxide layer using a DRIE Bosch process. The cavity created enables the micro-Newton force sensor to be inserted into the 1 mm^2 cavity to supply the desired force on the membrane.

The general fabrication process is identical for both membranes and is outlined in Fig. 7. The oxide layer, due to a different coefficient of thermal expansion than the crystalline silicon device layer, is under compressive stress and results in the Si/SiO$_2$ membrane buckling repeatedly inward once the handle layer is removed via the DRIE process. In an effort to develop a consistent, repeatable fabrication process, a series of 10 different fabrication runs were performed using a 16 element Si/SiO$_2$ membrane array to assess the fabrication process and verify device performance. In addition, five additional fabrication runs were performed using the same 16 element Si/SiO$_2$ membrane array with the Ti/Au metal layer added to the membrane surface to verify device performance. Overall, the fabrication process is very repeatable for either membrane type with nearly identical post fabrication results.
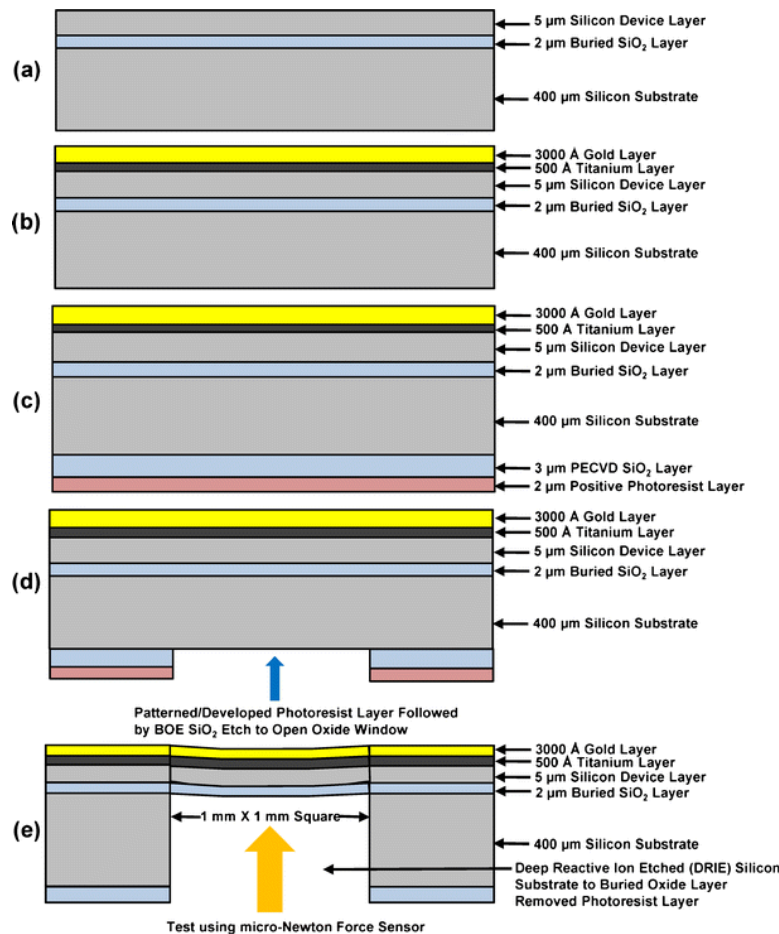
Fig. 7 Sequential fabrication of the multilayer material membrane, (**a**) illustrates the substrate wafer with a 2 μm buried oxide layer with a 5 μm Si device layer, (**b**) shows the evaporated metal layers (500 Å Ti, 3000 Å gold), (**c**) backside wafer preparation beginning with a 3 μm PECVD SiO₂ layer followed by a 2 μm thick photoresist layer for patterning, (**d**) Photoresist is patterned and developed to expose oxide layer which is then followed by a BOE etch to remove the oxide, and lastly, (**e**) the silicon substrate is DRIE through the backside window to the buried topside oxide layer, which acts as a natural etch stop. A micro-Newton force sensor is then inserted into the 1 mm × 1 mm cavity to supply the desired force on the membrane

Experimental Testing

To test the operation of the Si/SiO₂ membrane and the Si/SiO₂ Ti/Au membrane, three different experimental testing procedures were performed. The first testing sequence involved the use of an IFM to measure the peak deflections of the various membranes. The second set of testing involved the use of micro-Raman spectroscopy to measure the stress within the Si/SiO₂ membrane. The final set of tests involved load deflection tests which used a micro-Newton force sensor to physically deflect the Si/SiO₂ and the Si/SiO₂ Ti/Au membranes to measure the spring constant for each membrane type. Each testing procedure is outlined below with associated results.

Interferometric Microscope

To verify the out of plane deflection of the released Si/SiO₂ membrane, an IFM was used to measure the peak deflection of the membranes. Figure 8(a) illustrates a typical 2D deflection profile and Fig. 8(b) illustrates a typical 3D deflection image for the membrane which represents an axially

symmetric inverted dome. As shown in Fig. 8(c), the Si/SiO$_2$ membrane has a peak deflection of approximately 17.0 µm. A second membrane consisting of Si/SiO$_2$ with the additional Ti/Au metal on the membrane surface has a peak deflection of approximately 13.5 µm as shown in Fig. 8(d). This peak deflection reduction was expected based on the FEM analysis results obtained earlier. In general, the silicon device layer on top of the 2 µm thick oxide layer should inhibit the out of plane deflection, meaning the membrane should deflect into the cavity created by the DRIE etch. This in-cavity deflection held true for all cases; however, when the fabrication of the membrane included the addition of the metal Ti/Au layer, the inward deflection magnitude was reduced. A series of 5 Si/SiO$_2$ wafers and an additional 5 Si/SiO$_2$ with Ti/Au metal added on the device layer were fabricated. Each fabricated wafer consisted of the 16 element membrane array in which each membrane was measured using the IFM to determine the repeatability of the fabrication process as well as the consistency in membrane deflection. The average Si/SiO$_2$ membranes deflection measured 17.0 $\pm$ 0.5 µm while the Si/SiO$_2$ with the Ti/Au metal layer averaged approximately 13.5 $\pm$ 0.3 µm.
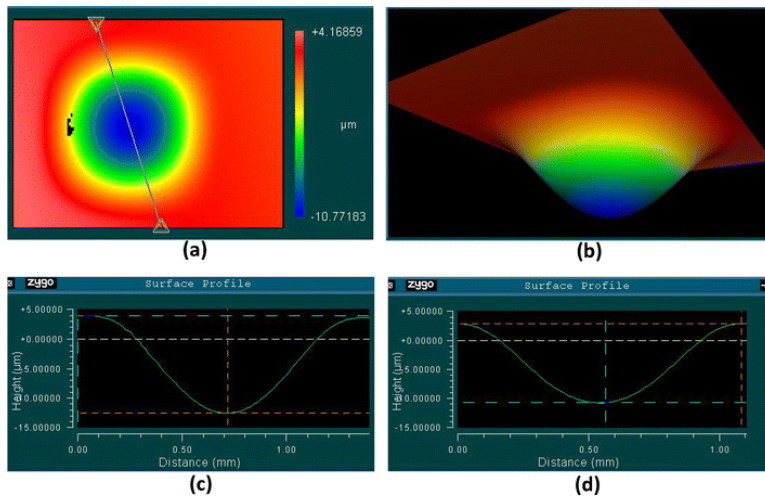

Fig. 8 IFM images illustrating the Si/SiO$_2$ membrane deflection upon release (**a**) provides the 2D image, (**b**) shows the 3D image of the membrane, (**c**) illustrates the ~17 µm deflection profile for the Si/SiO$_2$ membrane, and (**d**) illustrates the ~13.5 µm deflection profile for the Si/SiO$_2$ membrane with Ti/Au metal

Micro-Raman Spectroscopy

The mechanical properties of structural layers, in particular the stress and stress gradients are very important for proper device performance. This research builds on the understanding and behavior of thin film silicon structures as their scaled down in size. Several techniques have been used to characterize the strain in silicon thin films to include wafer curvature,[27] membrane load deflection,[28] interferometric measurements (IFM) of deflection and curvature and X-ray diffraction.[29] Previously, micro-Raman spectroscopy was used to measure residual and induced stresses in silicon MEMS structures.[30] Micro-Raman spectroscopy was selected since it has the advantage of being fast and nondestructive with micrometer spacial resolution. Several groups have shown micro-Raman spectroscopy is an effective technique for the measurement of mechanical stress in silicon[30,31,32,33,34,35,36,37,38] and silicon MEMS devices.[39,40,41,42,43,44,45,46]

In micro-Raman spectroscopy, laser light is focused on the sample through a microscope to a spot size of ~1 µm in diameter. A laser beam ($\lambda = 532\ nm$) is used to irradiate the sample and the scattered light, which carries the Raman signals, is collected and directed into a spectrometer. The spectrometer

measures the intensity of the Raman signal as a function of frequency. For an unstressed sample, the spectrometer measures a reference spectrum. Figure 9(a) shows a typical Raman spectrum for silicon which is used in this study. The Rayleigh scattering (laser line) is used as a reference to locally and individually calibrate each Raman spectrum. When the sample is placed in a stressed state, the Raman spectrum displays a shift in frequency with respect to the reference spectrum as shown in Fig. 9(b). This frequency shift is a result of residual or induced stress.
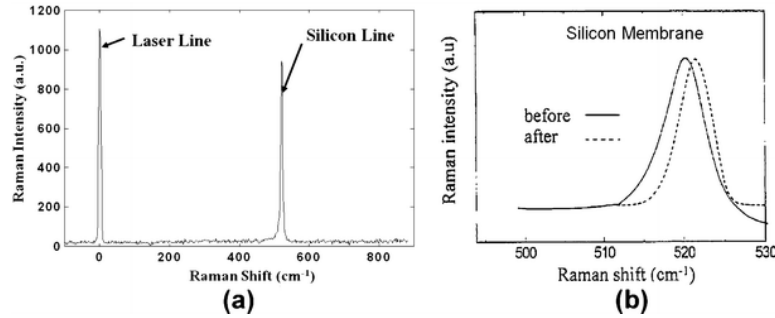

Fig. 9 (**a**) illustrates a typical Micro-Raman Spectroscopy profile for silicon showing both the Rayleigh (laser line) and the silicon line, and (**b**) illustrates a typical frequency shift due to stress in the silicon material

For this effort, micro-Raman spectroscopy was used to measure the residual stress in the released Si/SiO₂ membrane structure. The Raman spectra were obtained using a Renishaw inVia Raman microscope in backscattering mode. The Raman excitation source is an all solid-state, single frequency laser emitting at 532 nm. The laser power was limited to 1.8 mW at the sample to minimize sample heating. Scanning was accomplished using a stepping XYZ stage with a 1 μm resolution. Scans of the Si/SiO₂ membrane were accomplished by focusing the laser through a microscope objective, resulting in a spatial resolution of ~1 μm. Polarization was not used during the Raman stress measurements. The frequency shifts in the Raman spectra were found by fitting the Raman peak with a Lorentzian function with an error of approximately 0.1 Rcm^{-1}. The Raman shift was then referenced to the Rayleigh scattering line to account for any spectrometer variations.

Figure 10(a) shows an example 3D FEM mises stress image obtained from CoventorWare for the Si/SiO₂ membrane and identifies the stress magnitudes and locations across the membrane. The modeled membrane stress results indicate the peak stresses of approximately 340 MPa are located primarily at peak deflection locations (i.e. near the center of the membrane). In addition, the image indicates the corners of the square membrane cause an increased stress reflected toward the center of the membrane. From this model, a circular membrane could reduce this reflected stress, mitigating these high stress locations; however, the deflection of the membrane is ultimately controlled by the membrane thickness and the stress magnitudes within the material layers. Figure 10(b) is a comparison plot between the stress profile obtained from extracting a 2D stress profile from CoventorWare and a typical stress profile obtained from micro-Raman spectroscopy. As can be seen from Fig. 10(b), the micro-Raman stress profile compares favorably with the stress magnitudes and locations from the FEM model results. The micro-Raman spectroscopy stress profile also indicates peak stress near the center of the membrane and measured to be approximately 370 MPa. The stress profile shown in Fig. 10(b) is similar to the uniform loaded fixed-fixed beam stress profile shown in Fig. 4(b). The primary difference in the profiles are the stress and deflection magnitudes in the model as they only included a small uniformly distributed load which is extremely small when compared to the inherent forces due to the

residual stresses. In addition, the FEM stress images for the Si/SiO₂ membrane with the Ti/Au metal layer are nearly identical to the image shown in Fig. 10(a) with the exception of the stress magnitudes resulting from the added metal layers. A micro-Raman spectroscopy stress profile cannot be obtained for the metal layer due to the high reflection of the gold layer. On a side note, significantly higher stress values applied to the silicon device layer resulted in only minimal changes in the membrane deflection. Thus, as stated, the oxide layer dominates the overall deflection magnitude for this Si/SiO₂ membrane.
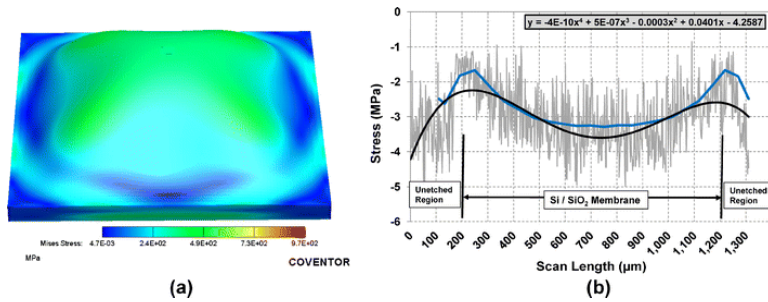

Fig. 10 (**a**) shows the Mises stress magnitudes and locations in the Si/SiO₂ membrane as modeled using CoventorWare, and (**b**) a comparison of the stress profile obtained from CoventorWare to the residual stress profile obtained using micro-Raman spectroscopy for the Si/SiO₂ membrane

Load Deflection Testing

All testing was performed on 1 mm² fabricated membranes in which the buckled oxide membrane is an axially symmetric dome that resembles the geometry of Fig. 3(a) if rotated around the k_2 spring. The load deflection plot obtained from a Si/SiO₂ membrane structure shown in Fig. 1(b) was obtained and compared to the disk cone spring[1] plot shown in Fig. 1(a). The load deflection tests were performed utilizing a calibrated capacitive force sensor mounted to a piezo-electric actuator having a 20 μm range with a resolution of .4μN at 30 Hz. The force sensor was displaced 200 nm at 500 ms intervals through the substrate into and away from the crown of the in-cavity deflected membrane. The produced membrane is on average 17 μm lower than the surrounding device layer. The membrane is bistable in that it could either be pushed into or out of the substrate and retain its position. As illustrated in Fig. 1(b), the load deflection plot consists of three regions of different rates. The first region demonstrates a "Hookean" linear spring return rate (positive spring constant), the second is a nearly zero spring return rate (constant force, a zero spring constant), and the third is a decreasing nonlinear spring return rate (negative spring constant). The load deflection curve shown in Fig. 1(b) for the Si/SiO₂ membrane shape was typical of other structures with similar geometry except for the extended zero stiffness region around the inflection point. This plot gives a general idea of the largest returnable deflection that was achievable without pop through. In comparison of the plots shown in Fig. 1, one immediately observes the similarities of the load deflection profiles for the two devices. The only real observable difference in the load profiles is that the large center disk spring results shown in Fig. 1(a) has load magnitudes in pounds and deflections in inches as compared to the micro load and nanometer deflections of the Si/SiO₂ membrane.

A second set of membranes were fabricated with the addition of thin film metallic layers (i.e. a 500 Å Ti and 3000 Å gold) being evaporated onto the silicon device layer which resulted in a reduced peak membrane deflection to approximately 13.5 μm. The load deflection test was repeated for this multi-stacked membrane and the associated profile is shown in Fig. 11 along with the profile obtained for the Si/SiO₂ membrane for ease of comparison. As shown in Fig. 11, the Si/SiO₂ with metal profile

demonstrates both a positive and negative linear stiffness where the inflection point is now much sharper and the negative stiffness portion has been highly linearized as compared to the Si/SiO$_2$ deflection profile. Curve fitting produces a spring constant of −39μn/nm (−390 N/m) over a 4 μm deflection range in the negative portion. A linear negative spring constant with a range of over 3 μm presents great possibilities. While improved sensitivity in accelerometers due to counteracting spring stiffness is an obvious use,[47] the prospect of vibration isolation of MEMS sensors in general has great potential.[48,49]
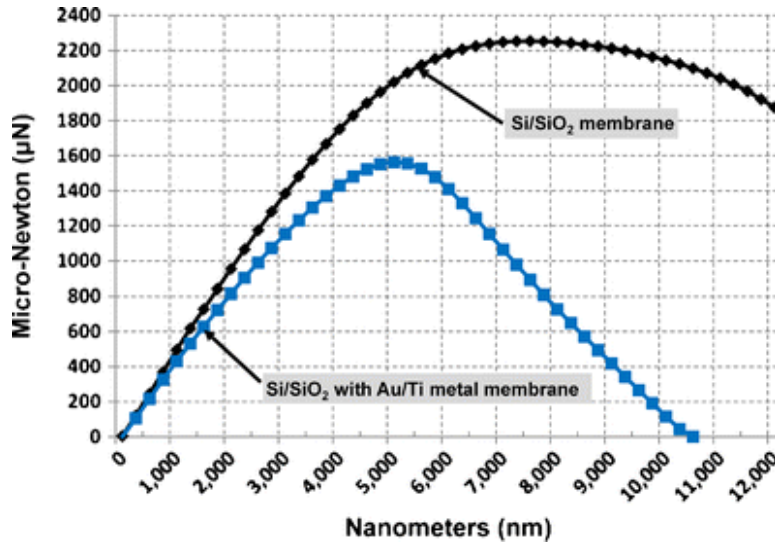

Fig. 11 Load deflection curves obtained for the Si/SiO$_2$ membrane, and the Si/SiO$_2$ membrane with a 500 Å Ti/3000 Å gold metal layer deposited on the membrane. As shown, the Si/SiO$_2$ membrane with metal provides a nearly linear positive and negative stiffness

Conclusion

Several different 16 element, 1 mm^2 membranes (Si/SiO$_2$ and Si/SiO$_2$ with Ti/Au metal layers) were successfully modeled, fabricated and tested. Both the peak membrane deflection and inherent residual stress levels were modeled and experimentally measured with nearly identical results. An IFM was used to measure the membrane deflections for the Si/SiO$_2$ and Si/SiO$_2$with Ti/Au metal layers with deflections measuring approximately 17.0 μm and 13.5 μm respectively. The reduced deflection was expected through our CoventorWare FEM model results. The residual stress in the Si/SiO$_2$ membrane was measured using micro-Raman spectroscopy to be approximately 370 MPa. The stress profile obtained closely resembles the analytical stress profile generated for a fixed-fixed microbridge with a small uniform, distributed load. In addition, the measured peak stress levels in the membrane closely match the FEM results of 340 MPa. Lastly, a micro-Newton force sensor was used to produce the load verse deflection profiles for the membranes. The Si/SiO$_2$ membrane force testing results in a positive linear stiffness with an inflection point holding nearly constant with a slight negative stiffness. Force testing results for the Si/SiO$_2$ membrane with the added Ti/Au metal layers results in both a linear positive and negative stiffness with a fairly sharp inflection point.

Notes

References

1. Almen JO, Laszlo A (1936) The uniform-section disk spring. Trans ASME 56:305–314
2. Sulfridge M, Saif T, Miller N, Meinhart M (2004) Nonlinear dynamic study of a bistable MEMS: model and experiment. J Microelectromech Syst 13:725–731
3. Joglekar MM, Pawaskar DN (2011) Closed-form empirical relations to predict the static pull-in parameters of electrostatically actuated microcantilevers having linear width variation. Microsys Technol 17:35–45
4. "How It Works." Minus K Technology. Web. (2010) <http://www.minusk.com/content/technology/how-it-works_passive_vibration_isolatior.html>
5. Guo ZY, Liu XS, Yang ZC, Shao QC, Lin LT, Xie H, Yan GZ (2010) Electrostatic isolation structure for linearity improvement of a lateral-axis tuning fork gyroscope, (MEMS). 2010 IEEE 23rd Int. Conf., 264–267
6. Baugher JP, Coutu RA Jr (2011) Micromechanical structure with stable linear positive and negative stiffness. Conf Proc Soc Exp Mech 4:137–143
7. Qiu J, Lang JH, Slocum AH (2001) A centrally-clamped parallel-beam bistable MEMS mechanism. The 14th IEEE International Conference on Micro Electro Mechanical Systems, MEMS 2001, 353–356
8. Kaltsas G, Nassiopoulou AG, Siakavellas M, Anastassikis E (1998) Stress effect on suspended polycrystalline silicon membranes fabricated by micromachining of porous silicon. Sens Actuators A 68:429–434
9. Howe RT, Boser BE, Pisano AP (1996) Polysilicon integrated microsystems: technologies and applications. Sens Actuators A 56:167–177
10. Maier-Schneider D, Köprülülü A, Ballhausen Holm S, Obermeier E (1996) Elastic properties and microstructure of LPCVD polysilicon films. J Micromech Microeng 6:436–446
11. Morshed S, Baldwin KE, Zhou B, Prorok BC (2009) Modifying geometry to enhance the performance of microcantilever-based acoustic sensors. Sensor Lett 7:38–41
12. Morshed S, Prorok BC (2007) Tailoring beam mechanics towards enhancing detection of hazardous biological species. Exp Mech 47:405–415
13. Guiming Z, Libo Z, Zhuangde J, Shuming Y, Yulong Z, Enze H, Rahman-Hebibul, Ziaopo W, Zhigang L (2011) Surface stress-induced deflection of a microcantilever with various widths and overall microcantilever sensitivity enhancement via geometry modification. J Phys D: Appl Phys 425402(44):1–11
14. Lakes RS, Lee T, Bersie A, Wang YC (2001) Extreme damping in composite materials with negative-stiffness inclusions. Nature 565–567
15. Wang YC, Lakes RS (2004) Extreme stiffness systems due to negative stiffness elements. Am J Phys 72:40–50

16. Handtmann M, Aigner R, Meckes A, Wachutka GKM (2002) Sensitivity enhancement of MEMS inertial sensors using negative springs and active control. Sens Actuators 97–98:153–160
17. Shigley JE, Mischke CR, Budynas RG (2004) Mechanical engineering design, 7th edn. McGraw-Hill, New York
18. Maenaka K (2008) MEMS inertial sensors and their applications. INSS 2008, 5th Intnl Conf on Networked Sensing Systems, 71–73
19. Tabata O, Kawahata K, Sugiyama S, Igarashi I (1989) Mechanical property measurements of thin films using load-deflection of composite rectangular membranes. Sen Actuators 20:135–141
20. Pan JY, Lin P, Masech F, Senturia SD (1990) Werification of FEM analysis of load-deflection methods for measuring mechanical properties of thin films. Tech Dig IEEE Solid-State Sensors & Actuators Workshop 1990, Hilton Head Island, SC, 70–73
21. Maier-Schneider D, Maibach J, Obermeier E (1995) A new analytical solution for the load-deflection of square membranes. J Microelectromech Syst 4:238–241
22. Timoshenko S, Woinowsky-Krieger S (1959) Theory of plates and shells. McGraw-Hill, New York
23. Pilkey WD (1994) Formulas for stress, strain, and structural matrices. Wiley & Sons
24. CoventorWare® User's Manual (2010) Coventor, Inc., 4000 Centregreen Way, Cary, NC
25. De Wolf I (1996) Micro-Raman Spectroscopy to study local mechanical stress in silicon integrated circuits. Semicond Sci Technol 11:139–154
26. Best SR (2005) Detection of residual stress in multi-crystalline silicon wafers using swept-sine frequency response data. Dissertation, University of South Florida, Tampa, Florida
27. Koester DA, Mahadevan R, Hardy B, Markus KW (1999) MUMPs™ Design Handbook Rev. 5, Cronos Integrated Microsystems, 3021 Cornwallis Road, Research Triangle Park, NC
28. Zou Q, Li Z, Liu L (1995) New methods for measuring mechanical properties of thin films in micromachining: beam pull-in (VPI) method and long beam deflection (LBD) method. Sens Actuators A 48:137–143
29. Anastassakis E, Pinczuk A, Burstein E, Pollak FH, Cardona M (1970) Effect of static uniaxial stress on the Raman spectrum of silicon. Solid State Commun 8:133–138
30. Starman LA, Lott JA, Amer MS, Cowan WD, Busbee JD (2003) Stress characterization of MEMS microbridges by micro-Raman spectroscopy. Sens Actuators A 104:107–116
31. De Wolf I (1996) Micro-Raman spectroscopy to study local mechanical stress in silicon integrated circuits. Semicond Sci Technol 11:139–154
32. Siakavellas M, Anastassikis E, Koltsas G, Nassiopoulos AG (1998) Micro-Raman characterization of stress distribution within free standing mono- and poly-crystalline silicon membranes. Microelectron Eng 41(42):469–472
33. Talaat H, Negm S, Schaffer HE, Kaltsas G, Nassiopoulos AG (2000) Micro-Raman analysis of polysilicon membranes deposited on porous silicon channels. J Non-Crystalline Solids 266–269:1345–1349
34. Wu X, Yu J, Ren T, Liu L (2007) Micro-Raman spectroscopy measurement of stress in silicon. Microelectron J 38:87–90
35. Anaya J, Prieto AC, Martinez O, Torres A, Martin-Martin A, Jimenez J, Rodriquez A, Sangrador J, Rodriquez T (2011) Si and Si_xGe_{1-x} NWs studied by Raman spectroscopy. Physica Status Solidi C 8:1307–1310
36. Gustafson PA, Haris SJ, O'Neill AE, Waas AM (2006) Measurement of biaxial stress states in silicon using micro-raman spectroscopy. J Appl Mech Trans ASME 73:745–751

37. Kang Y, Qiu Y, Lei Z, Hu M (2005) An application of Raman spectroscopy on the measurement of residual stress in porous silicon. Opt Lasers Eng 43:847–855
38. Harris SJ, O'Neill AE, Yang W, Gustafson P, Boileau J, Weber WH, Majumdar B, Ghosh S (2004) Measurement of the state of stress in silicon with micro-Raman spectroscopy. J Appl Phys 96:7195–7201
39. Srikar VT, Swan AK, Ünlü MS, Goldberg BB, Spearing SM (2003) Micro-Raman measurement of bending stresses in micromachined silicon flexures. J Microelectromechanical Systems 12:779–787
40. Abel MR, Wright TL, King WP, Graham S (2007) Thermal metrology of silicon microstructures using raman spectroscopy. IEEE Trans Components Packaging Technol 30:200–208
41. Jungchul L, Beechem T, Wright TL, Nelsonand BA, Graham S, King WP (2006) Electrical, thermal, and mechanical characterization of silicon microcantilever heaters. J Microelectromechanical Systems 15:1644–1655
42. Taniyama A, Hirai Y, Sugano K, Tabata O, Ikehara T, Tsuchiya T (2011) Local stress analysis of single crystalline silicon resonator using micro Raman spectroscopy, IEEE 24th Intnl Conf on MEMS, 449–452
43. Xue C, Zheng L, Zhang W, Zhang B, Jian A (2006) A dynamic stress analyzer for microelectromechanical systems (MEMS) based on Raman spectroscopy. J Raman Spectrosc
44. Pan X, Tan CW, Miao J, Kasim J, Shen Z, Xie E (2009) The stress analysis of Si MEMS devices by Micro-Raman technique. Thin Solid Films 517:4905–4908
45. De Wolf I, Kalicinski S, De Coster J, Oprims H (2009) Methods to measure mechanical properties of NEMS and MEMS: challenges and pitfalls. Material Research Society Symposium Proceedings, 1185
46. Miyatake T, Pezzotti G (2011) Tensor-resolved stress analysis in silicon MEMS device by polarized Raman spectroscopy. Phys Status Solidi A 208:1151–1158
47. Ya'akobovitz A, Krylov S (2010) Toward sensitivity enhancement of MEMS accelerometers using mechanical amplification mechanism. Sens J IEEE 10:1311–1319
48. Lee SH, Lee SW, Najafi K (2007) A generic environment-resistant packaging technology for MEMS. Solid-State Sens Act Microsys Conf, TRANS 2007 Intnl, 335–338
49. Dean R, Flowers G, Hodel S, MacAllister K, Horvath R, Matras A (2002) Vibration isolation of MEMS sensors for aerospace applications. Proc. of the IMAPS Int. Conf. & Exhib. on Adv. Pack. & Sys., 166–170